

Image enhancement based on intuitionistic fuzzy sets theory

ISSN 1751-9659
 Received on 21st January 2016
 Revised 10th March 2016
 Accepted on 25th March 2016
 E-First on 24th May 2016
 doi: 10.1049/iet-ipr.2016.0035
 www.ietdl.org

He Deng^{1,2}, Xianping Sun¹, Maili Liu¹, Chaohui Ye¹, Xin Zhou¹ ✉

¹State Key Laboratory of Magnetic Resonance and Atomic and Molecular Physics, National Center for Magnetic Resonance in Wuhan, Wuhan Institute of Physics and Mathematics, Chinese Academy of Sciences, Wuhan 430071, People's Republic of China

²Hubei Key Laboratory of Medical Information Analysis & Tumor Diagnosis and Treatment, Wuhan 430074, People's Republic of China

✉ E-mail: xinzhou@wipm.ac.cn

Abstract: Enhancement of images with weak edges faces great challenges in imaging applications. In this study, the authors propose a novel image enhancement approach based on intuitionistic fuzzy sets. The proposed method first divides an image into sub-object and sub-background areas, and then successively implements new fuzzification, hyperbolisation, and defuzzification operations on each area. In this way, an enhanced image is obtained, where the visual quality of region of interest (ROI) is significantly improved. Several types of images are utilised to validate the proposed method with respect to the enhancement performance. Experimental results demonstrate that the proposed algorithm not only works more stably for different types of images, but also has better enhancement performance, in comparison to conventional methods. This is a great merit of such design for discerning specific ROIs.

1 Introduction

In a quite few occasions, optical or medical images have poor contrast, and are degenerated with different types of noise, or blurred owing to the physical properties of imaging devices and image transmission [1]. Thus, image enhancement is one of inevitable tasks in image processing [2–6], intending to selectively highlight or inhibit specific information, adjust the contrast, smooth the region of interest (ROI), or sharpen the edges or fine structures in an image. Current state-of-art enhancement algorithms include the histogram equalisation [3, 4], non-linear unsharp masking [5], wavelet transform [6], fuzzy sets [1, 2], and so on. However, the enhancement of images that have weak edges is still difficult in computer vision and pattern recognition.

According to the assumption that a uniformly distributed greyscale histogram will result in the best visual contrast, histogram equalisation methods hold the dominant position in the field of image enhancement [3, 4]. However, some drawbacks hinder their development, such as the washed out effect, inability to preserve edges, and non-preservation of brightness [7]. Moreover, the ambiguity and uncertainty are unavoidably produced during the image acquisition or transmission. Accordingly, a valid way portraying such image should utilise human knowledge expressed heuristically. This is highly non-linear and cannot be represented by conventional mathematical modelling [8].

Recently, fuzzy sets theory [9] has attracted great attention in image processing [1, 2, 10–13], because fuzzy techniques are non-linear and knowledge based. These algorithms can process imperfect data derived from vagueness and ambiguity rather than randomness. Consequently, fuzzy sets- or fuzzy logic-based methods are properly suited to automatically adjust the contrast, and then improve the visual quality of an image [7, 13, 14]. Nevertheless, classical fuzzy enhancement methods proposed in [2] encounter some difficulties. One is that the grey-level range of the output image is almost unchanged, which suggests that these methods are unsuitable for enhancing those degraded images with less grey levels and low contrasts. The other is that the range of membership function is not a normalisation form [15]. Furthermore, an optimal condition of enhancement is none the less absent.

Compared with conventional fuzzy sets, intuitionistic fuzzy sets take into account more uncertainties in the form of membership

function (viz., membership degree, non-membership degree, and hesitation degree). These fuzzy sets are more conformable to aspects of human decision making [16]. In recent years, intuitionistic fuzzy sets have been widely used in various applications [17–19], such as image denoising [17] and image fusion [19]. Therefore, we propose a novel enhancement approach based on intuitionistic fuzzy sets to adaptively enhance images with weak edges in this paper.

Our method has two advantages. The first is that the membership function is founded by using the restricted equivalence function (REF), and the range of membership function is normalised to [0, 1]. It is suitable to discriminate different parts of an image. The second advantage is that the new fuzzification, hyperbolisation, and defuzzification operations are consecutively implemented on respective object and background areas of each sub-image. These implementations can be parallel processed. By applying such method on brain tumour magnetic resonance (MR) images, mammograms, small target infrared images, and non-destructive testing (NDT) images, it shows that the designed method not only works robustly for enhancing different types of images, but also has a good enhancement performance.

The organisation of the rest of this paper is as follows. Section 2 reviews fuzzy sets, intuitionistic fuzzy sets, and the framework of fuzzy image enhancement. An intuitionistic fuzzy sets-based enhancement method is constructed in Section 3. Experimental results and discussions are given in Section 4. Section 5 presents conclusions and perspectives.

2 Related work

This section briefly discusses the theories of fuzzy sets and intuitionistic fuzzy sets, and the framework of fuzzy image enhancement [1, 2, 9, 16]. These construct the basis of the novel enhancement scheme.

2.1 Fuzzy sets

Let U be a space of points (objects) set, i.e. $U = \{u\}$, where u denotes a generic element of U . A fuzzy set $A = \{(u, \mu_A(u), \nu_A(u)) \mid u \in U\}$ in U is characterised by a membership function $\mu_A(u)$, where $\mu_A(u): U \rightarrow [0, 1]$, $u \rightarrow \mu_A(u)$, and $\nu_A(u) = 1 - \mu_A(u)$. The function $\mu_A(u)$ associates a real number in the interval [0, 1] with each point

in U . The value of $\mu_A(u)$ denotes the membership degree at u in A , and the value of $\nu_A(u)$ is the non-membership degree. The nearer the value of $\mu_A(u)$ to unity, the higher will be the grade of membership degree [9].

An image U of size $M \times N$ with L grey levels can be defined as an array of fuzzy singletons that indicate the membership degree of each pixel point. The definition of the membership value depends on the specific needs in applications. Provided that $\mu_A(u_{ij})$ represents the degree of brightness, the membership degree proposed in [2] could be described as

$$\mu_A(u_{ij}) = \Psi(u_{ij}) = \left[1 + \frac{(u_{\max} - u_{ij})}{d} \right]^{-e}, \quad (1)$$

where u_{\max} is the maximum grey level in an image, e and d denote the exponential and denominational fuzzifiers that regulate the amount of greyness ambiguity in a membership plane. Proper values for e are 1 and 2. Then d can be obtained from the crossover point g of the membership function ($\mu(g) = 0.5$) [1].

2.2 Intuitionistic fuzzy sets

Each element in the membership plane is represented by a membership degree, while the non-membership degree is equal to 1 minus the membership degree according to the conventional fuzzy sets [9]. However, the membership degree expressed by human being seldom coincides with the non-membership degree as the complement to unity [16]. Intuitionistic fuzzy sets can reflect that fact, which introduces a term of intuitionistic fuzzy index or hesitation degree owing to the lack of knowledge or ‘personal error’ [20, 21].

Under the conception of hesitation degree, an intuitionistic fuzzy set A in a finite U can be represented as (see (2)) where functions $\mu_A(u)$, $\nu_A(u)$, and $o_A(u)$ are the membership degree, non-membership degree, and hesitation degree, respectively. Some intuitionistic fuzzy generators can be utilised to form an intuitionistic fuzzy set, e.g. Sugeno-type intuitionistic fuzzy generator [16, 20].

2.3 Framework of fuzzy image enhancement

Fuzzy image processing generally has three phases [1, 2]. (i) Fuzzification Ψ , i.e. an input data U (e.g. features, histograms, grey levels) is converted into a membership plane. (ii) Operation Γ , i.e. some proper operator is applied in the membership plane for special applications (e.g. enhancement [2, 7, 10], thresholding [16]). (iii) Defuzzification Φ , i.e. if necessary, the adjusted membership plane is inversely converted into the characteristic plane, such as features, histograms, and grey levels. Therefore, the output X of the fuzzy system for an input U is given by the following processing chain:

$$X = \Phi(\Gamma(\Psi(U))), \quad (3)$$

The main difference to other methodologies in image processing is that the diversity of fuzzy logic, fuzzy sets, intuitionistic fuzzy sets, and fuzzy measure theories are conveniently adopted to modify or aggregate membership values, classify data, or make decisions using fuzzy inference in the membership plane [1], rather than in the image plane.

3 Image enhancement based on intuitionistic fuzzy sets

Since intuitionistic fuzzy sets are more conformable for human being to make decisions, an image enhancement scheme based on intuitionistic fuzzy sets is proposed to improve images with weak edges in this section.

3.1 Membership function

A fuzzy set necessitates precisely assigning a membership degree to each element of the set. We adopt a REF to construct the membership function of an intuitionistic fuzzy set.

If ϑ_1 and ϑ_2 are two automorphisms in a unit interval, a REF will be denoted as [16, 21]

$$\text{REF}(x, y) = \vartheta_1^{-1}(1 - |\vartheta_2(x) - \vartheta_2(y)|), \quad x \in [0, 1], y \in [0, 1], \text{ with } c(x) = \vartheta_2^{-1}(1 - \vartheta_2(x)), \quad (4)$$

where REF: $[0, 1] \times [0, 1] \rightarrow [0, 1]$, and $c(x)$ is a strong negation.

Assume that $\vartheta_1(x) = \log[x(\exp(1)-1) + 1]$ and $\vartheta_2(x) = x^2$, $x \in [0, 1]$, (4) will become

$$\text{REF}(x, y) = \frac{[\exp(1 - |x + y| \cdot |x - y|) - 1]}{(\exp(1) - 1)}, \quad (5)$$

Then, (5) satisfies the conditions for a REF. The proofs are displayed as follows:

- i. $\text{REF}(x, y) = \text{REF}(y, x)$, for all $x, y \in [0, 1]$.
- ii. When $x = y$, $\text{REF}(x, y) = 1$, and vice versa.
- iii. When $x = 0, y = 1$, or $x = 1, y = 0$, $\text{REF}(x, y) = 0$, and vice versa.
- iv. $\forall x, y \in [0, 1]$, then $\text{REF}(x, y) = \text{REF}(c(x), c(y))$, where c is a strong negation (see Appendix 1).
- v. $\forall x \leq y \leq z \in [0, 1]$, then $\text{REF}(x, y) \geq \text{REF}(x, z)$ and $\text{REF}(y, z) \geq \text{REF}(x, z)$ (see Appendix 2).

Since REFs are local functions [21], REFs can be adopted as local indexes to measure some specific property of an image. We utilise REFs to measure the difference between a pixel and its neighbourhood region. The membership function $\mu \rightarrow [0, 1]$ is defined as

$$\begin{aligned} \mu_A(u_{ij}) &= \Psi(u_{ij}) = \text{REF}(u_{ij}, v) \\ &= \frac{[\exp(1 - |u_{ij} + v| \cdot |u_{ij} - v|) - 1]}{(\exp(1) - 1)}, \end{aligned} \quad (6)$$

where u_{ij} is the grey value at point (i, j) , and v denotes some property of the neighbourhood region.

Since a foreground (object) or background area has correlations in both spatial and frequency domains, the membership function should represent the belonging of a point to the foreground or background area. Thus, it is necessary to separate an image into foreground and background areas for enhancement. For a pixel involved in a foreground or background area, its membership function is expressed as

$$\begin{aligned} \mu_A(u_{ij}) &= \begin{cases} \Psi_1(u_{ij}), & \text{if } u_{ij} \geq u_A^c \\ \Psi_2(u_{ij}), & \text{if } u_{ij} < u_A^c \end{cases} = \\ &= \begin{cases} \frac{[\exp(1 - |u_{ij} + m_0| \cdot |u_{ij} - m_0|) - 1]}{(\exp(1) - 1)}, & \text{if } u_{ij} \geq u_A^c \\ \frac{[\exp(1 - |u_{ij} + m_1| \cdot |u_{ij} - m_1|) - 1]}{(\exp(1) - 1)}, & \text{if } u_{ij} < u_A^c \end{cases}, \end{aligned} \quad (7)$$

where m_0/m_1 denotes the average grey of the foreground/background area, and u_A^c is a certain threshold that separates the image into the foreground and background areas.

The REF proposed in [16] is $\text{REF}(x, y) = [\exp(1 - |x - y|) - 1] / (\exp(1) - 1)$, different from (5). However, the membership function according to [16] may arouse some questions. The analysis is displayed as follows. Fig. 1a shows a local area of size 7×7 with

$$A = \{(u, \mu_A(u), \nu_A(u), o_A(u)) | u \in U\}, \quad \text{s.t. } \mu_A(u) + \nu_A(u) + o_A(u) = 1, \quad (2)$$

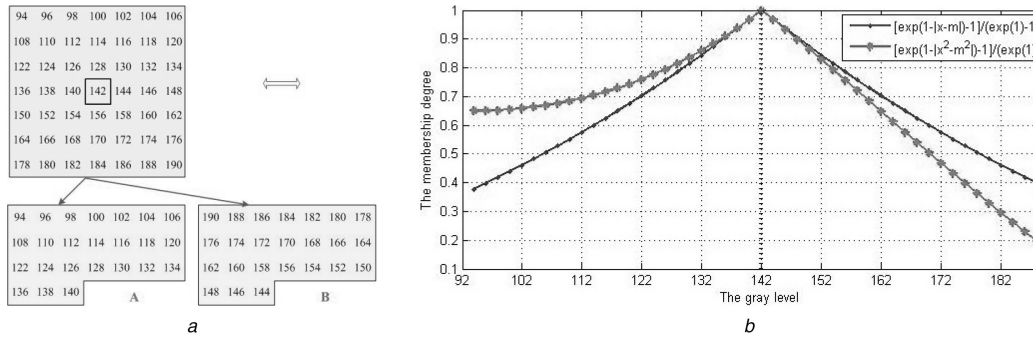


Fig. 1 Local object or background area and the graphs according to different membership functions

a Local grey area with size of 7×7

b Graphs of different membership functions

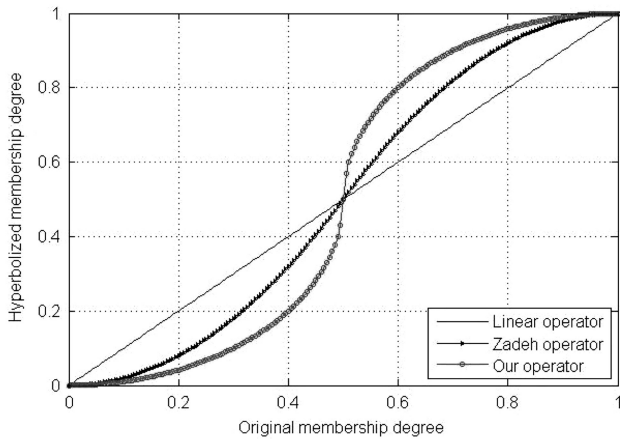


Fig. 2 Relationship between the original and hyperbolised membership degrees based on the linear, Zadeh, and the presented hyperbolisation operators

49 grey levels. The average grey of this area is 142 (viz., black rectangular box). The graph of the membership function by using Eq. (8) in [16] is shown in Fig. 1b, denoted as the deltoid curve. The circle curve in Fig. 1b is the graph of the membership function according to (7). In Fig. 1, the x -axis denotes the grey level, the y -axis denotes the membership degree, and the black dotted line is the mean of the area.

The deltoid curve is symmetrical for the dotted line, while that property is invalid for the circle curve, as shown in Fig. 1b. If the area is decomposed into two parts, denoted as A and B (the pixel positions in B are properly rearranged, as shown in the lower part of Fig. 1a), the distance between A and B by using Eq. (9) in [16] will be zero (see Appendix 3 for Eqs. (8) and (9)). This implies that A is so much like B , which is inconsistent with their original grey comparison. Accordingly, the membership function based on Eq. (8) in [16] may produce some troubles in particular applications, such as segmentation or classification. However, the membership degree according to (7) first increases non-linearly and then decreases linearly, as shown in Fig. 1b. The divergence between A and B is 1.8840 rather than 0, which is more suitable to

discriminate the parts A and B (the parameter in Eq. (8) in [16] is chosen as 0.8).

3.2 Hyperbolisation

After the construction of membership function, a new hyperbolisation operator is presented to modify the membership degree of each pixel point involved in object or background areas. In this section, we consider the following hyperbolisation function:

$$\mu'_A(x) = \begin{cases} a - \sqrt{(a+x)(a-x)}, & \text{if } 0 \leq x < a \\ a + \sqrt{(2-a-x)(x-a)}, & \text{if } a \leq x \leq 1 \end{cases} \quad (8)$$

where μ'_A is the hyperbolised membership degree, x is the original membership degree, and a is the positive constant.

Fig. 2 shows the relationship between the original and hyperbolised membership degrees according to the linear, Zadeh, and our hyperbolisation functions ($a=0.5$). The linear and Zadeh hyperbolisation functions [1, 2] are described as follows:

$$\hat{\mu}_A(x) = x, x \in [0, 1], \quad \tilde{\mu}_A(x) = \begin{cases} 2x^2, & \text{if } 0 \leq x < 0.5 \\ 1 - 2(1-x)^2, & \text{if } 0.5 \leq x \leq 1 \end{cases} \quad (9)$$

The membership degree is unchanged when the linear hyperbolisation is used. The Zadeh hyperbolisation function reduces the fuzziness of a set A by augmenting the values of $\mu_A(x)$ which are above a and lessening those which are below it, as shown in Fig. 2. Through our operator, the difference of two parts in the hyperbolised membership plane is further widened. This is useful to improve the contrast of specific ROI. Then we utilise this hyperbolisation operator to hyperbolise membership degrees in each object or background membership plane, viz. (see (10)) where $\mu_O(u_{ij})$ and $\mu_B(u_{ij})$ denote original membership degrees in the object and background membership plane, μ_O^{\min} and μ_O^{\max} denote the minimum and maximum membership degrees in the object membership plane, while μ_B^{\min} and μ_B^{\max} denote the minimum and maximum membership degrees in the background membership plane.

$$\mu'_A(u_{ij}) = \begin{cases} \Gamma_1(\mu_O(u_{ij})), & u_{ij} \in O \\ \Gamma_2(\mu_B(u_{ij})), & u_{ij} \in B \end{cases} = \begin{cases} \mu_O(u_A^c) - \sqrt{(\mu_O(u_A^c) + \mu_O(u_{ij}))(\mu_O(u_A^c) - \mu_O(u_{ij}))}, & \mu_O^{\min} \leq \mu_O(u_{ij}) \leq \mu_O(u_A^c) \\ \mu_O(u_A^c) + \sqrt{(2 - \mu_O(u_A^c) - \mu_O(u_{ij}))(\mu_O(u_{ij}) - \mu_O(u_A^c))}, & \mu_O(u_A^c) < \mu_O(u_{ij}) \leq \mu_O^{\max} \\ \mu_B(u_A^c) - \sqrt{(\mu_B(u_A^c) + \mu_B(u_{ij}))(\mu_B(u_A^c) - \mu_B(u_{ij}))}, & \mu_B^{\min} \leq \mu_B(u_{ij}) \leq \mu_B(u_A^c) \\ \mu_B(u_A^c) + \sqrt{(2 - \mu_B(u_A^c) - \mu_B(u_{ij}))(\mu_B(u_{ij}) - \mu_B(u_A^c))}, & \mu_B(u_A^c) < \mu_B(u_{ij}) \leq \mu_B^{\max} \end{cases} \quad (10)$$

where $\mu_O(u_A^c) = \frac{[\exp(1 - |u_A^c + m_0| \cdot |u_A^c - m_0|) - 1]}{(\exp(1) - 1)}$, $\mu_B(u_A^c) = \frac{[\exp(1 - |u_A^c + m_1| \cdot |u_A^c - m_1|) - 1]}{(\exp(1) - 1)}$

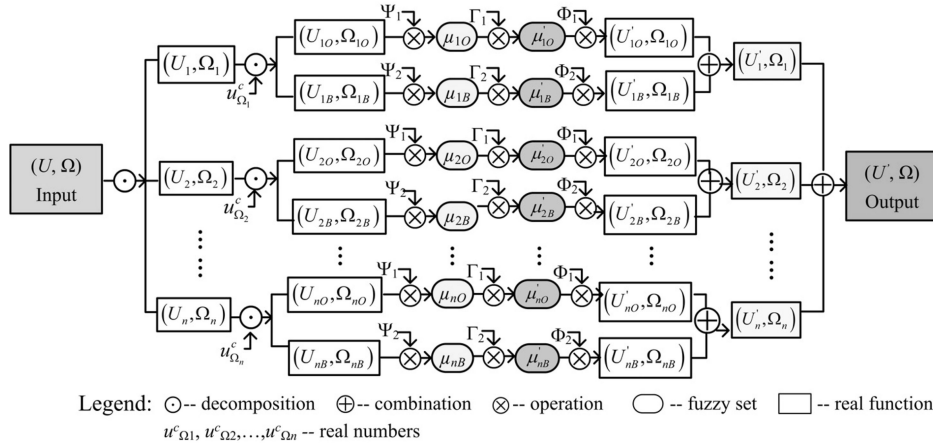


Fig. 3 Block diagram of the proposed fuzzy image enhancement method

For the points whose grey levels are near to the average grey of the object or background area in an image, the presented hyperbolisation operator augments the belonging of these points to the area. On the other hand, the operator lessens the belonging of those points to the object or background area, whose grey levels are far from the average grey of the area.

3.3 Defuzzification

If necessary, the hyperbolised membership degrees need to be inversely converted into the pixel levels through the defuzzification operation. The defuzzification can be described as

$$u'_{ij} = \begin{cases} \Phi_1(\mu'_O(u_{ij})), & u_{ij} \in O \\ \Phi_2(\mu'_B(u_{ij})), & u_{ij} \in B \end{cases} =$$

$$\begin{cases} [m_0^2 + (1 - \log(1 + (\exp(1) - 1)\mu'_O(u_{ij})))^{0.5}], & m_0 \leq u_{ij} \leq u^{\max} \\ [m_0^2 - (1 - \log(1 + (\exp(1) - 1)\mu'_O(u_{ij})))^{0.5}], & u_A^c \leq u_{ij} < m_0 \\ [m_1^2 + (1 - \log(1 + (\exp(1) - 1)\mu'_B(u_{ij})))^{0.5}], & m_1 \leq u_{ij} < u_A^c \\ [m_1^2 - (1 - \log(1 + (\exp(1) - 1)\mu'_B(u_{ij})))^{0.5}], & u^{\min} \leq u_{ij} < m_1 \end{cases} \quad (11)$$

where u'_{ij} denotes the new grey value, u^{\min} and u^{\max} denote the minimum and maximum grey values in the original image plane.

3.4 Proposed enhancement method

The process of the proposed image enhancement algorithm is illustrated in Fig. 3. Without loss of generality, let (U, Ω) be an image plane with L grey levels, i.e. $(U, \Omega): U \rightarrow [0, L-1], \Omega \rightarrow [1, M] \times [1, N]$. The proposed method is initially employed to divide an image into several windows, $(U_i, \Omega_i), i = 1, 2, \dots, n$, where $\Omega_i \cap \Omega_j = \emptyset, i \neq j, \cup \Omega_i = \Omega$, and n is the number of windows. The window size is usually set to be 1/1, 1/2, or 1/4 of the image size. Thus, each window (U_i, Ω_i) is segmented into the object area Ω_{iO} and background area Ω_{iB} by a threshold $u^c_{\Omega_i}$, that is, $\Omega_i = \Omega_{iO} \cup \Omega_{iB}$. We can obtain the following relationship:

$$\Omega = (\Omega_{1O} \cup \Omega_{1B}) \cup (\Omega_{2O} \cup \Omega_{2B}) \cup \dots \cup (\Omega_{nO} \cup \Omega_{nB}) = \left(\bigcup_{i=1}^n \Omega_{iO} \right) \cup \left(\bigcup_{i=1}^n \Omega_{iB} \right). \quad (12)$$

From Sections 3.1 to 3.3, the fuzzification Ψ_k , hyperbolisation Γ_k , and defuzzification Φ_k ($k = 1, 2$) are successively performed on

the object and background areas in each window. As a result, a new image plane (U', Ω) is obtained, whose quality is improved.

4 Results and discussions

In this section, we use four classes of images to demonstrate the effectiveness and practicality of the proposed method, i.e. brain tumour MR images, mammograms, small target infrared images, and NDT images. In our method, an image is first divided into several windows (sub-images). Then, we adopt Otsu's thresholding method [22] to separate each window into object and background areas. Undoubtedly, other thresholding methods can be integrated with the proposed method, which is out of the scope of this work.

4.1 Brain tumour MR images

MR can non-invasively offer good soft-tissue contrast and high spatial resolution images, which is the most frequently used technique for radiologists and surgeons to detect and diagnose brain tumours. Different MR sequences are used to image different interesting structures, as shown in Fig. 4. T1-weighted images (e.g. Fig. 4a) are usually used for the structural analysis. Fig. 4b shows a T2-weighted image, where abnormal regions (e.g. the oedema and tumour) and the cerebrospinal fluid (CSF) are bright against the dark normal brain tissues. In order to separate the brain tumour from the focal oedema, a T1-enhanced image (gadolinium-DTPA) is necessary, as shown in Fig. 4c. Since the free water signal is suppressed in a T2-FLAIR (T2-weighted with fluid-attenuated inversion recovery) image (see Fig. 4d), the focal oedema is easily separated from the CSF. The arrows in Fig. 4 denote the interesting regions.

Through our method, the corresponding enhanced results of Figs. 4a–d are shown in Figs. 4e–h. These original and enhanced images are evaluated by several radiologists and surgeons. Compared with the original MR images, they agree that: (i) the focal oedema is more conspicuous in Fig. 4e, and the contrast between the focal oedema and anatomic structure of the brain is more obvious; (ii) in Fig. 4f, the focal oedema is highlighted, and the mass effect (e.g. the midline and brain fold are pressed and pushed shift) is more obvious; (iii) the active tumour ingredients are clearer, as shown in Fig. 4g. The contrast between the active tumour ingredients and the normal brain tissue is evidently improved; (iv) the influence of free water, CSF, and necrotic cystic are eliminated, and the focal oedema is more intact and clearer, as shown in Fig. 4h.

Figs. 5a–d display another original T1-weighted, T2-weighted, T1-enhanced, and T2-FLAIR brain tumour MR images. The focal oedemas are phanerous in Figs. 5b and d, while the active tumour ingredients are invisible in images under different imaging modes. Through our method, the corresponding enhanced results are shown in Figs. 5e–h, respectively. Compared with original MR images, the contrast and the focal oedema in Figs. 5e–h are more conspicuous and clearer. Thus, it is helpful to discriminate and diagnose the focal oedema and brain tumour.

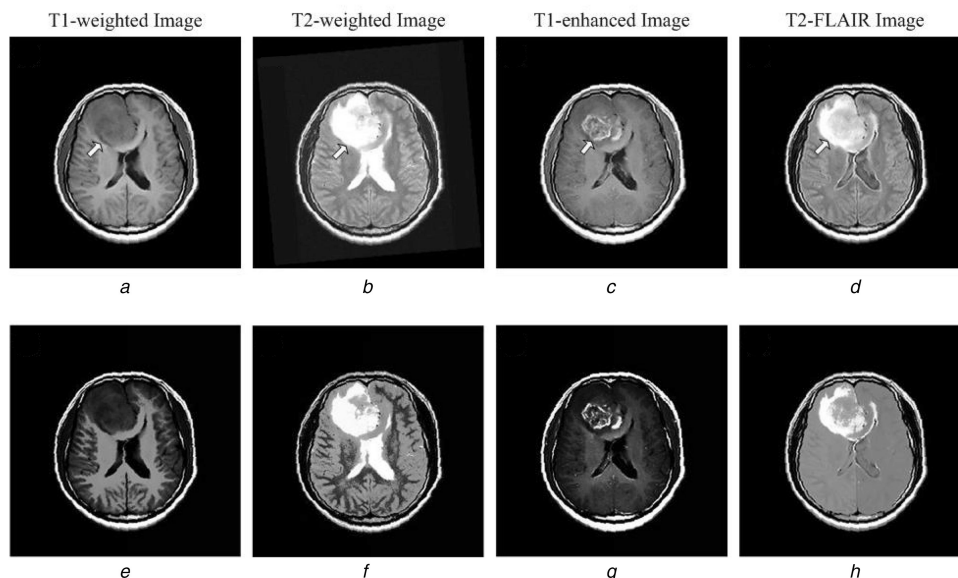


Fig. 4 Representative brain tumour MR images (upper) and the corresponding enhanced results (lower) obtained by using the proposed method
a, e T1-weighted image
b, f T2-weighted image
c, g T1-enhanced image
d, h T2-FLAIR image

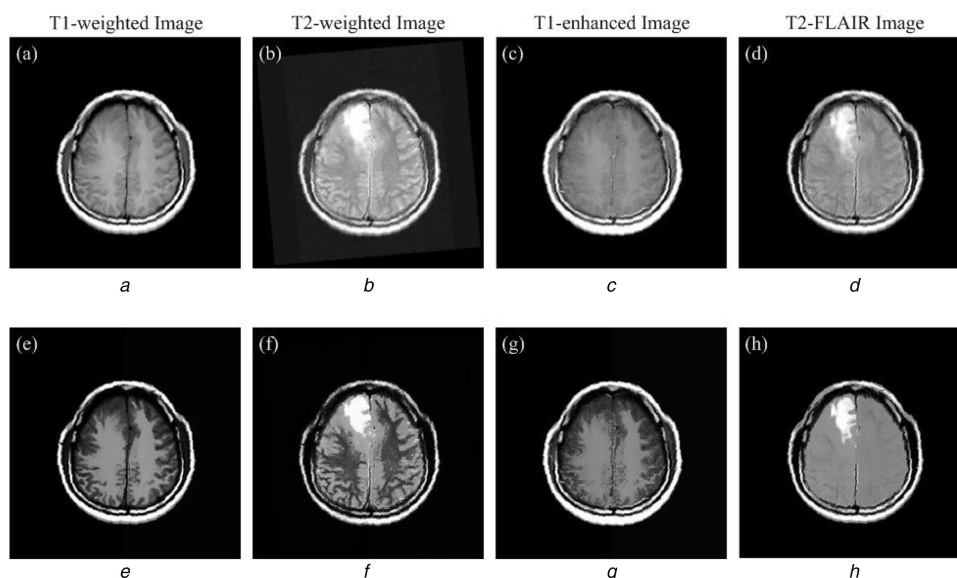


Fig. 5 Other brain tumour MR images (upper) and the enhanced results (lower) based on our method
a, e T1-weighted image
b, f T2-weighted image
c, g T1-enhanced image
d, h T2-FLAIR image

We adopt the measure of enhancement by entropy (EMEE) [23] to measure the quality of original and enhanced images. EMEE is based on a Weber-law-based contrast measure. EMEE measure first divides an image into some blocks with size of $p \times q$, then calculates the average value of measure results of all blocks in the entire image. EMEE can be defined as

$$EMEE_{pq} = -\frac{1}{pq} \sum_{s=1}^p \sum_{t=1}^q \left[\beta \left(\frac{G_{\max}}{G_{\min}} \right)^\beta \ln \left(\frac{G_{\max}}{G_{\min}} \right) \right], \quad (13)$$

where β is the constant, G_{\max} and G_{\min} are the maximum and minimum of intensity values in blocks, respectively.

For Figs. 4 and 5, Table 1 lists EMEE values of original and enhanced MR images, where a higher value suggests better enhancement performance. From Table 1, we can see that the enhanced images have higher EMEE values than the original ones.

Table 1 Comparison of EMEE measure results

	Fig. 4				Fig. 5			
original	0.8904	1.0026	0.4968	1.0377	0.4757	0.7284	0.4444	0.6028
our method	1.5225	1.5222	1.3981	1.2406	0.9459	1.1667	1.1099	0.8800

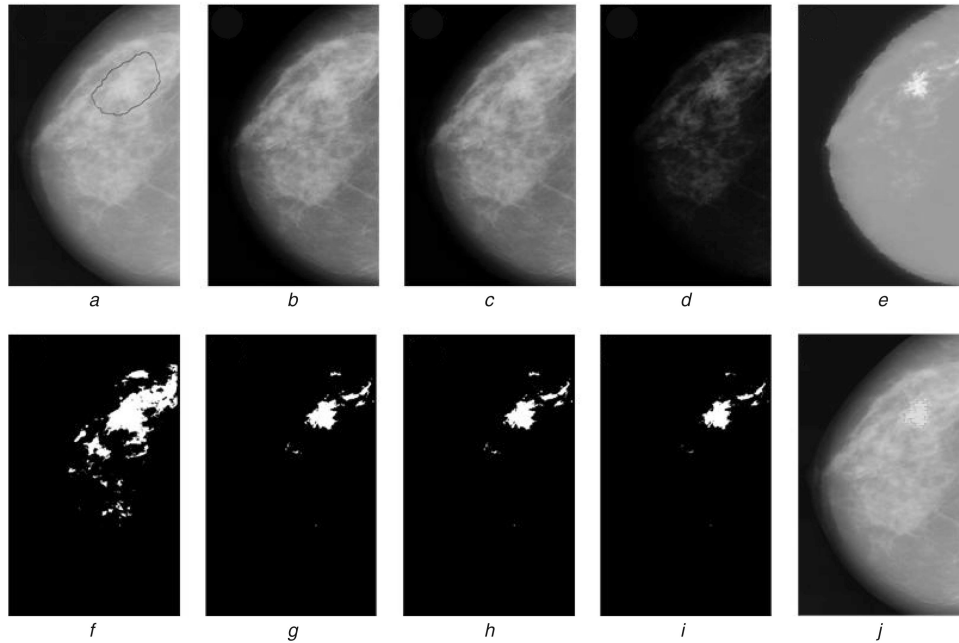


Fig. 6 Mammogram enhancement

a Original mammogram

b–e Enhanced results obtained by using the FHHM, λ -EM, NLFM, and our method

f–i Thresholding of a–d

j Thresholding of e added mammogram

4.2 Mammograms

Breast cancer is the chief cause of death in women among the ages of 35–55 years. However, screened mammograms are generally degraded by various types of noise, or blurred owing to the physical properties of imaging devices. This makes it difficult to distinguish and diagnose breast cancers. Consequently, it is necessary to improve the image quality, aiming to enhance the contrast of specific regions in mammograms without influencing the acquisition process or burdening the hardware costs.

An original mammogram is shown in Fig. 6a, where the black curve denotes the location of a mass and is not part of the processing. We can see that the contrast between the mass and surrounding normal tissues is very obscure. Through the fuzzy histogram hyperbolisation method (FHHM) [1], λ -enhancement method (λ -EM) [24], non-linear filter method (NLFM) [5], and the proposed method, the corresponding filtered results are shown in Figs. 6b–e. Comparing Fig. 6a–e, it can be seen that the FHHM and λ -EM methods slightly enhance the mass region. The NLFM method improves the contrast of the mass region, but it fail to provide the edge of mammogram. Fig. 6e provides the clear shape of mass and edge of mammogram. Figs. 6f–i denote the thresholding of specific ROI of Figs. 6a–d. The thresholding of Fig. 6e is added to the original mammogram, as shown in Fig. 6j. Fig. 6 indicates that our method outperforms the others since the abnormal regions are very clear and easily discernible.

Some objective measures can measure the enhancement performance of different methods, including Michelson law measure of enhancement (AME) and Michelson law measure of enhancement by entropy (AMEE) [25]. AME and AMEE measures divide an image into blocks with size of $m \times n$, and then calculate the average values of the measure results of all blocks in the entire image. The definitions of AME and AMEE are

$$AME_{mn} = -\frac{1}{mn} \sum_{s=1}^m \sum_{t=1}^n \left[20 \ln \left(\frac{F_{\max} - F_{\min}}{F_{\max} + F_{\min}} \right) \right],$$

$$AMEE_{mn} = -\frac{1}{mn} \sum_{s=1}^m \sum_{t=1}^n \left[\alpha \left(\frac{F_{\max} - F_{\min}}{F_{\max} + F_{\min}} \right)^\alpha \ln \left(\frac{F_{\max} - F_{\min}}{F_{\max} + F_{\min}} \right) \right], \quad (14)$$

where α is the constant, F_{\max} and F_{\min} are the maximum and minimum of intensity values in blocks, respectively.

For each measure, a higher score indicates the better enhancement performance. Table 2 lists the measure results obtained by using the FHHM, λ -EM, NLFM, and our method. Based on the scores, the proposed method gives the best overall visual quality with an AME score of 115.5410 and an AMEE score of 0.3299. This demonstrates that our method shows good performance in improving the contrast of specific regions.

4.3 Small target infrared images

Due to the long imaging distance, an infrared target is with small size without concrete shape and texture, and it is usually buried in low signal-to-clutter ratio (SCR) background clutters and noise [26, 27]. This produces great difficulties in the target detection. For an image with size of 128×128 , the size of small target possibly ranges from 1×1 to 5×5 pixels. Thus, the aim of enhancement for this image is to highlight the target and suppress the background as possible.

Fig. 7a shows a dim small target submerged in the complex sea-sky background. This suggests that it is impossible to directly detect the target from the background clutters. Some small target detection methods are used for comparison, including the maximum background prediction model (MBPM) [28], the top-hat filter (THT) [27], and the local contrast measure (LCM) [29]. For the representative image (viz., Fig. 7a), Figs. 7b–e show the filtered results obtained by using the MBPM, THT, LCM, and our

Table 2 Comparison of AME and AMEE measure results based on different algorithms

	Original	FHHM	λ -EM	NLFM	Our method
AME	60.6837	51.6923	51.6923	22.3831	115.5410
AMEE	0.3182	0.2654	0.2654	0.1570	0.3299

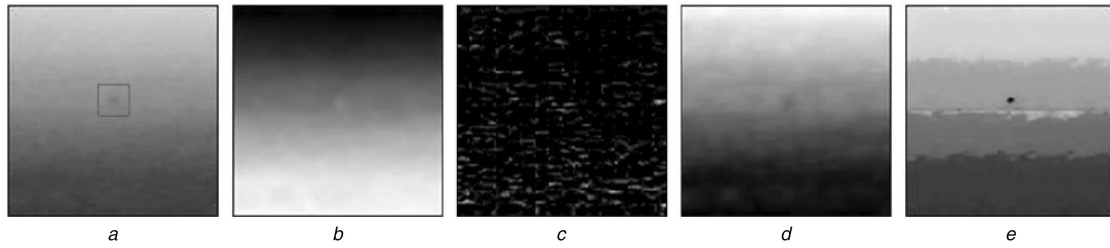


Fig. 7 Enhancement of a dim small target infrared image under sea-sky background

a Original image

b–e Different filtered results obtained by using the MBPM, THT, LCM, and our method

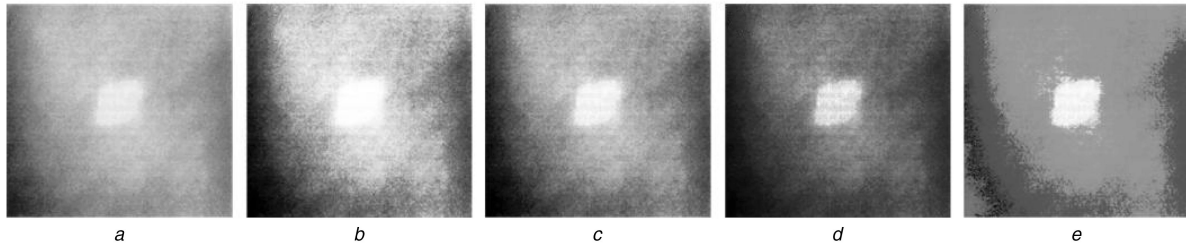


Fig. 8 Enhancement of NDT-1 image

a Original GFRP image

b–e Different enhanced results obtained by using the FRM, FHHM, λ -EM, and our method

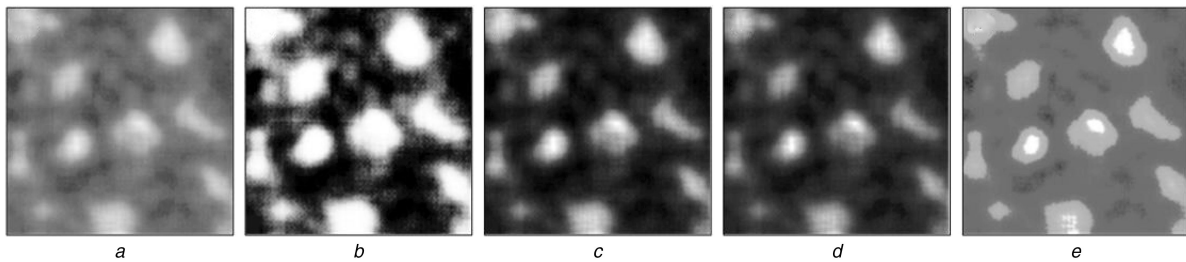


Fig. 9 Enhancement of NDT-2 image

a Original cell image

b–e Different enhanced results obtained by using the FRM, FHHM, λ -EM, and our method

method. It can be seen that the target is still obscure in Figs. 7b–d. This produces great trouble in the detection from these images. However, the target is clearer in Fig. 7e, in comparison to Figs. 7a–d. The layers of the target, sky, and sea are visibly distinct in Fig. 7e, which results in high contrast between the target and background. Consequently, the target in Fig. 7e is easily detected.

SCR is used to represent the difficulty in degree of small target detection. The SCR is

$$SCR = \frac{|m_t - m_b|}{\sigma_b} \quad (15)$$

where m_t denotes the average grey of the target, m_b and σ_b denote the average and standard deviation of grey values in the neighbouring region around the target, respectively.

As a general rule, the higher the SCR value of a small target image, the easier will be the detection of targets. Table 3 lists SCR and AMEE values obtained by using the MBPM, THT, LCM, and our method. This indicates that the target is most easily detected in Fig. 7e with a SCR score of 5.4005 and a AMEE score of 0.2167. Considering Fig. 7 and Table 3, the target is difficult to be detected as before by using the MBPM, THT, and LCM methods.

4.4 NDT images

NDT is widely used in science and industry to evaluate the properties of a material, component, or system without causing damage [30]. In this section, two real NDT images (denoted as NDT-1 and NDT-2) are adopted to evaluate the enhancement performance of the proposed method, as shown in Figs. 8a and 9a. One image represents a defective thermal image of glass-fibre reinforced plastics (GFRP) composite material. Its size is 246×227 . The other is a cell image with size of 133×133 . The similar feature in two NDT images is strong noise, and with weak edges. Thus, denoising and edge enhancing are chief tasks in the enhancement of such image.

For NDT-1 image, the grey levels of the defective region are similar, so the output image through the contrast adjustment should not alter that similarity while enlarging the difference between the defective and circumambient normal regions. Figs. 8b–e show the enhanced results obtained by using the fuzzy relaxation method (FRM) [14], FHHM, λ -EM, and our method, respectively. Comparing Figs. 8a–d, it can be seen that the grey similarity of the defective region is scarcely changed, but the grey difference between the defective and normal regions is lessened. This implies that the recognition of those defective regions is non-trivial in Figs. 8b–d. However, that grey difference in Fig. 8e is enlarged,

Table 3 Comparison of SCR values based on different algorithms

	Original	MBPM	THT	LCM	Our method
SCR	1.2404	0.4227	0.5465	0.5365	5.4005
AMEE	0.2088	0.1876	0	0.1737	0.2167

Table 4 Comparison of AME and AMEE measure results based on different algorithms

		Original	FRM	FHHM	λ -EM	Our method
NDT-1	AME	48.3436	36.5907	36.3998	32.7655	52.1148
	AMEE	0.2782	0.2370	0.2414	0.2300	0.2817
NDT-2	AME	43.3887	19.9894	20.3164	26.3100	55.9483
	AMEE	0.2675	0.1197	0.1553	0.1920	0.2870

while preserving the similar grey levels in the defective region. This results in an easy work to recognise the defective region.

The grey levels in cell regions have considerable variability, as shown in Fig. 9a. Thus, the grey diversity in cell regions should be remained in the enhancement results. The enhancement results obtained by using the FRM, FHHM, λ -EM, and our method are shown in Figs. 9b–e, respectively. We can see that the grey variety in cell regions is disappeared in Figs. 9b–d. The cell edges are still weak in Figs. 9c and d. As for the grey diversity remaining and cell edges enhancing, Fig. 9e is superior to Figs. 9b–d.

Both Figs. 8 and 9 clearly show how the enhancement algorithms change fine details in images. Their AME and AMEE measure results are listed in Table 4. It draws a conclusion that our method is superior to the others since it improves the contrast and visual quality of the images. The enhanced results obtained by using our method have no detail information loss. These are useful for detecting ROIs.

5 Conclusion

This paper proposes a novel fuzzy image enhancement approach based on intuitionistic fuzzy sets, aiming to enhance images with weak edges. The proposed approach divides an image into several sub-images consecutively followed by new fuzzification, hyperbolisation, and defuzzification operations implemented on respective object and background areas of each sub-image. The implementation can be in parallel processing. Four types of images are adopted to verify the enhancement performance of the proposed method, including brain tumour MR images, mammograms, small target infrared images, and NDT images. Experimental results demonstrate that the proposed method works robustly and has a good enhancement performance. This is useful for easily detecting specific ROIs. In the future, we will improve the flexibility of the proposed method for some specific applications. We will also further improve the robustness of our method for noisy images.

6 Acknowledgments

This work was supported by the Natural Science Foundation of China (61471355, 81227902), and the China Postdoctoral Science Foundation (2014M560636, 2015T80856).

7 References

- [1] Tizhoosh, H.R.: 'Fuzzy technique in image processing' (Spring-Verlag, Berlin, Heidelberg, 2000), Ch.5, pp. 137–146
- [2] Pal, S.K., King, R.A.: 'Image enhancement using smoothing with fuzzy sets', *IEEE Trans. Syst. Man Cybern.*, 1981, **11**, pp. 494–501
- [3] Wang, Y., Chen, Q., Zhang, B.M.: 'Image enhancement based on equal area dualistic sub image histogram equalization method', *IEEE Trans. Consum. Electron.*, 1999, **45**, pp. 68–75
- [4] Chen, S.D., Ramli, A.R.: 'Minimum mean brightness error bi-histogram equalization in contrast enhancement', *IEEE Trans. Consum. Electron.*, 2003, **49**, pp. 1310–1319
- [5] Panetta, K., Zhou, Y.C., Aghaian, S., et al.: 'Nonlinear unsharp masking for mammogram enhancement', *IEEE Trans. Inf. Technol. Biomed.*, 2011, **15**, pp. 918–928
- [6] Cho, D., Bui, T.D.: 'Fast image enhancement in compressed wavelet domain', *Signal Process.*, 2014, **98**, pp. 295–307
- [7] Raju, G., Nair, M.S.: 'A fast and efficient color image enhancement method based on fuzzy-logic and histogram', *Int. J. Electron. Commun.*, 2014, **68**, pp. 237–243
- [8] Liu, P.Y., Li, H.X.: 'Fuzzy techniques in image restoration research-a survey', *Int. J. Comput. Cogn.*, 2004, **2**, pp. 131–149
- [9] Zadeh, L.A.: 'Fuzzy sets', *Inf. Control*, 1965, **8**, pp. 338–353
- [10] Russo, F.: 'Recent advances in fuzzy techniques for image enhancement', *IEEE Trans. Instrum. Meas.*, 1998, **47**, pp. 1428–1434
- [11] Yang, C., Lu, L.J., Lin, H.P., et al.: 'A fuzzy-statistics-based principal component analysis (FS-PCA) method for multispectral image enhancement and display', *IEEE Trans. Geosci. Remote Sens.*, 2008, **46**, pp. 3937–3947

- [12] Wu, D.R.: 'Approaches for reducing the computational cost of interval type-2 fuzzy logic systems: overview and comparisons', *IEEE Trans. Fuzzy Syst.*, 2013, **21**, pp. 80–99
- [13] Hanmandlu, M., Jha, D.: 'An optimal fuzzy system for color image enhancement', *IEEE Trans. Image Process.*, 2006, **15**, pp. 2965–2966
- [14] Li, H., Yang, H.S.: 'Fast and reliable image enhancement using fuzzy relaxation technique', *IEEE Trans. Syst. Man Cybern.*, 1989, **19**, pp. 1276–1281
- [15] Peng, D.L., Xue, A.K.: 'Degraded image enhancement with applications in robot vision'. Proc. of IEEE ICSMC, 2005, pp. 1837–1842
- [16] Chaira, T.: 'Intuitionistic fuzzy segmentation of medical images', *IEEE Trans. Biomed. Eng.*, 2010, **57**, pp. 1430–1436
- [17] Ananthi, V.P., Balasubramaniam, P.: 'A new image denoising method using interval-valued intuitionistic fuzzy sets for the removal of impulse noise', *Signal Process.*, 2016, **121**, pp. 81–93
- [18] Ejegwa, P.A., Akowe, S.O., Otene, P.M., et al.: 'An overview on intuitionistic fuzzy sets', *Int. J. Sci. Technol. Res.*, 2014, **3**, pp. 142–145
- [19] Ananthi, V.P., Balasubramaniam, P.: 'Image fusion using interval-valued intuitionistic fuzzy sets', *Int. J. Image Data Fusion*, 2015, **6**, pp. 249–269
- [20] Bustunche, H., Barrenechea, E., Pagola, M.: 'Restricted equivalence functions', *Fuzzy Sets Syst.*, 2006, **157**, pp. 2333–2346
- [21] Szmidt, E., Kacprzyk, J.: 'Entropy for intuitionistic fuzzy set', *Fuzzy Sets Syst.*, 2001, **118**, pp. 467–477
- [22] Otsu, N.: 'A threshold selection method from gray level histograms', *IEEE Trans. Syst. Man Cybern.*, 1979, **9**, pp. 62–66
- [23] Aghaian, S.S., Panetta, K.A., Grigoryan, A.M.: 'Transform-based image enhancement algorithms with performance measure', *IEEE Trans. Image Process.*, 2001, **10**, pp. 367–382
- [24] Tizhoosh, H.R., Krell, G., Michaelis, B.: ' λ -enhancement: contrast adaptation based on optimization of image fuzziness'. Proc. of IEEE FSP, 1998, pp. 1548–1553
- [25] Aghaian, S.S., Silver, B., Panetta, K.A.: 'Transform coefficient histogram-based image enhancement algorithms using contrast entropy', *IEEE Trans. Image Process.*, 2007, **16**, pp. 741–758
- [26] Deng, H., Liu, J.G., Chen, Z.: 'Infrared small target detection based on modified local entropy and EMD', *Chin. Opt. Lett.*, 2010, **8**, pp. 24–28
- [27] Deng, H., Wei, Y.T., Tong, M.W.: 'Small target detection based on weighted self-information map', *Infrared Phys. Technol.*, 2013, **60**, pp. 197–206
- [28] Huang, K., Mao, X.: 'Detectability of infrared small targets', *Infrared Phys. Technol.*, 2010, **53**, pp. 208–217
- [29] Philip, C.L., Li, H., Wei, Y.T., et al.: 'A local contrast method for small infrared target detection', *IEEE Trans. Geosci. Remote Sens.*, 2014, **51**, pp. 574–581
- [30] Deng, H., Wei, Y.T., Zhao, G., et al.: 'Integration of local information-based transition region extraction and thresholding', *Infrared Phys. Technol.*, 2014, **66**, pp. 103–113

8 Appendix

8.1 Appendix 1

Let $c: [0,1] \rightarrow [0,1]$. c is a strong negation if it satisfies the following properties [16]: (i) $c(0) = 1$ and $c(1) = 0$; (ii) $c(x) \leq c(y)$, if $x \geq y$ (monotonicity); (iii) $c(x)$ is continuous; (iv) $c(x) < c(y)$, for $x > y$ for all $x, y \in [0,1]$ (involutivity); (v) $c(c(x)) = x$, for all $x \in [0,1]$.

Proof: According to (4) and (5), $c(x)$ can be described as

$$\left. \begin{aligned} c(x) &= \vartheta_2^{-1}(1 - \vartheta_2(x)) \\ \vartheta_2(x) &= x^2, x \in [0, 1] \end{aligned} \right\} \rightarrow c(x) = \sqrt{1 - x^2}, \quad x \in [0, 1]$$

Then, the above equation satisfies the conditions for strong negation, which is as follows:

- $c(0) = 1$ and $c(1) = 0$;
- $2)c'(x) = (\sqrt{1 - x^2})' = (-x/\sqrt{1 - x^2}) < 0, \quad \forall x \in (0, 1)$, then $c(x)$ is a monotonically decreasing function in the interval $[0,1]$;
- $c(x)$ is a continuous function;
- $c(x)$ is involutive according to the second conclusion;
- $\forall x \in [0,1], c(c(x)) = \sqrt{1 - (c(x))^2} = \sqrt{x^2} = x$.

Thus

$$\begin{aligned} \text{REF}(c(x), c(y)) &= \frac{[\exp(1 - |(c(x))^2 - (c(y))^2|) - 1]}{(\exp(1) - 1)} \\ &= \frac{[\exp(1 - |y^2 - x^2|) - 1]}{(\exp(1) - 1)} = \text{REF}(x, y) \end{aligned}$$

Therefore, (5) satisfies the fourth condition for REF. □

8.2 Appendix 2

Proof: Let $t = |x^2 - y^2|$, $\forall x, y \in [0, 1]$, in (5), then $t \in [0, 1]$. Thus, (5) becomes

$$\text{REF}(t) = \frac{(\exp(1 - t) - 1)}{(\exp(1) - 1)}$$

Then, $\text{REF}(t)$ is a monotonically decreasing function in the interval $[0, 1]$. For $\forall x, y, z \in [0, 1]$, and $x \leq y \leq z$, then $x^2 \leq y^2 \leq z^2$. Then $|x^2 - y^2| \leq |x^2 - z^2|$ and $|y^2 - z^2| \leq |x^2 - z^2|$. Let $t_1 = |x^2 - y^2|$, $t_2 = |x^2 - z^2|$, $t_3 = |y^2 - z^2|$, then $t_1 \leq t_2$ and $t_3 \leq t_2$, which imply that $\text{REF}(t_2) \leq \text{REF}(t_1)$ and $\text{REF}(t_2) \leq \text{REF}(t_3)$. Thus, $\text{REF}(x, z) \leq \text{REF}(x, y)$, and $\text{REF}(x, z) \leq \text{REF}(y, z)$.

Therefore, (5) satisfies the fifth condition for REF. □

8.3 Appendix 3

Equation (8) in [16] is described as

$$\mu(u_{ij}) = \begin{cases} \frac{(\exp(1 - |u_{ij} - m_0|) - 1)}{(\exp(1) - 1)}, & u_{ij} \leq t \\ \frac{(\exp(1 - |u_{ij} - m_1|) - 1)}{(\exp(1) - 1)}, & u_{ij} > t \end{cases}$$

Equation (9) in [16] is described as

$$\begin{aligned} D_{\text{IFS}}(A, B) &= \sum_i \sum_j \left[\begin{aligned} &2 - (1 - \mu_A(u_{ij}) + \mu_B(s_{ij}))\exp(\mu_A(u_{ij}) - \mu_B(s_{ij})) \\ &- (1 - \mu_B(s_{ij}) + \mu_A(u_{ij}))\exp(\mu_B(s_{ij}) - \mu_A(u_{ij})) \\ &+ 2 - (1 - \mu_A(u_{ij}) - o_A(u_{ij}) + \mu_B(s_{ij}) + o_B(s_{ij})) \\ &\exp(\mu_A(u_{ij}) + o_A(u_{ij}) - \mu_B(s_{ij}) - o_B(s_{ij})) \\ &- (1 - \mu_B(s_{ij}) - o_B(s_{ij}) + \mu_A(u_{ij}) + o_A(u_{ij})) \\ &\exp(\mu_B(s_{ij}) + o_B(s_{ij}) - \mu_A(u_{ij}) - o_A(u_{ij})) \end{aligned} \right] \end{aligned}$$

where $A = \{(u, \mu_A(u_{ij}), \nu_A(u_{ij}), o_A(u_{ij})) | u_{ij} \in A\}$ and $B = \{(s, \mu_B(s_{ij}), \nu_B(s_{ij}), o_B(s_{ij})) | s_{ij} \in B\}$ are two intuitionistic fuzzy images.